



Dynamic modeling of absorption/desorption closed-loop including periphery

Mike Bothe, Iman Hami Dindar, Nicole Lutters, Eugeny Y. Kenig^{*}

Chair of Fluid Process Engineering, Paderborn University, Paderborn, Germany

ARTICLE INFO

Keywords:

Dynamic behavior
Closed-loop
Chemical absorption
Malfunction
Emergency
Periphery

ABSTRACT

Reactive absorption is one of the most important separation processes used within the chemical industry to address the environmental protection challenges. In this process, undesirable gaseous components are captured by chemical reaction in a solvent and the loaded solvent is then regenerated in the desorption unit. Both process steps take place simultaneously and strongly interact resulting in a very complex process behavior. To ensure stable and safe process operation, even in presence of instabilities/malfunctions, understanding of the dynamic process behavior is essential. In this work, the development of a novel dynamic model for simulation of a reactive absorption/desorption process in a closed-loop configuration including the periphery of the plant is presented. The validation of the model is accomplished based on two dynamic experiments carried out in our own pilot plant. The deviations between experimental and simulated outlet gas concentrations are below 10% for both experiments.

1. Introduction

Absorption units are usually complemented by desorption columns to regenerate the solvent, thus building a closed-loop configuration. As column internals, various packings, both structured and random, are applied to ensure a large contact area between the gas and the solvent. Packed columns also contain liquid distributors that help to realize even distribution of the solvent. Furthermore, the periphery of the plant comprises several heat exchangers (HEs) and pipelines. Each of the plant components, as those shown in a typical configuration in Fig. 1, influences the overall process behavior. Unforeseen changes in the process or plant conditions can lead to hazardous situations. Examples of such situations are flooding of the columns, a large increase in pressure or an insufficient absorption of toxic gas components, which can be very dangerous. In order to avoid the hazardous situations, understanding of the dynamic process behavior is necessary.

Different groups studied dynamics of absorption processes using both modeling and experimental analysis. Kvamsdal et al. (2009) theoretically investigated the dynamic process behavior for a stand-alone absorption column using an equilibrium stage approach. They claimed that their model had been validated. However, this was done only for a steady-state process, with the experimental data from the MEA campaign carried out at the University of Texas at Austin, USA

(Dugas, 2006). Ziaei et al. (2011) developed a dynamic rate-based model for a stand-alone desorption column. Due to the high temperatures in the column, the reactions were considered as instantaneous. Again, the dynamic model could not be validated due to lacking experimental data on transient process behavior. Gáspár and Cormoş (2011) investigated the absorption/desorption closed-loop process using the rate-based approach. They considered the reaction kinetics only for the “main” reaction between MEA and CO₂, while the influence of further reactions encountered in the system was neglected. Bilyok et al. (2012) and Åkesson et al. (2012) took all reactions into account. However, the reactions were treated as instantaneous (in both the desorption and absorption column). Due to the lower temperatures in the absorption column, this assumption is questionable. None of the works cited above considered the influence of the periphery and non-separating column internals like liquid distributors on the process dynamics. Harun et al. (2012) included the reboiler and a HE in their closed-loop model. The absorption/desorption process in the columns was modeled with the rate-based approach using enhancement factors; in contrast, the HE was considered as an equilibrium stage. The influence of the liquid distributors or the pipelines on the process dynamics was neglected. During the last five years, publications have largely been focused on data-driven models governing transient absorption/desorption process behavior. However, the necessary data were generated with non-validated and mostly too simplified physical concepts (Wu et al., 2020).

^{*} Corresponding author.

E-mail address: eugeny.kenig@upb.de (E.Y. Kenig).

<https://doi.org/10.1016/j.compchemeng.2022.107960>

Received 28 February 2022; Received in revised form 1 August 2022; Accepted 10 August 2022

Available online 12 August 2022

0098-1354/© 2022 Elsevier Ltd. All rights reserved.

Nomenclature

A :	area, m^2
a :	specific gas-liquid interfacial area, m^2/m^3
b :	plate width, m
c :	molar concentration, mol/m^3
c_p :	specific heat capacity, $J/(kg\ K)$
D :	diffusion coefficient, m^2/s
e :	relative deviation, %
d_h :	hydraulic diameter, m
F :	Faraday's constant, $9.65 \times 10^4\ C/mol$
G :	gas-phase molar flow rate, mol/s
h :	molar enthalpy, J/mol
k :	overall heat transfer coefficient, $W/(m^2\ K)$
k_r :	reaction rate constant, diverse
K :	equilibrium constant, -
K_i :	phase distribution coefficient, -
L :	liquid-phase molar flow rate, mol/s
m :	number of passages in a plate HE, -
\dot{m} :	mass flow rate, kg/s
N_{ch} :	number of channels, -
N_{plate} :	number of plates, -
n :	number of stages, -
n_i :	molar flux of component i , $mol/(m^2\ s)$
NC :	number of components, -
Nu :	Nusselt number, -
p :	pressure, Pa
\dot{Q} :	heat flow rate, W
R_i :	total component reaction rate, $mol/(m^3\ s)$
R :	gas constant, $J/(mol\ K)$
r :	number of reactions, -
r_i :	equivalent reaction rate, $mol/(m^3\ s)$
t :	time, s
T :	temperature, K
U :	specific molar holdup, mol/m
V :	volume, m^3
x :	coordinate, m
x_i :	liquid-phase mole fraction of component i , mol/mol
y :	coordinate, m
y_i :	gas-phase mole fraction of component i , mol/mol
z :	coordinate, m
z_i :	ionic charge of component i , -

Greek letters

α :	convective heat transfer coefficient, $W/(m^2\ K)$
γ :	activity coefficient, -
δ :	thickness, m
η :	dimensionless film coordinate, -
λ :	thermal conductivity, $W/(m\ K)$

ν :	stoichiometric coefficient, -
ρ :	density, kg/m^3
ϕ :	volumetric holdup, m^3/m^3
φ :	electrical potential, V
Ψ :	absorption efficiency, %

Subscripts

back:	backward
ch:	channel
e:	educt
eff:	effective
for:	forward
gas:	gas-phase
liq:	liquid-phase
i:	component
in:	inlet flow
n:	stage
out:	outlet flow
p:	product
pg:	passages
plate:	plates
t:	total

Superscripts

c:	cold fluid, secondary side
G:	gas phase
Gb:	gas bulk phase
Gf:	gas film phase
h:	hot fluid, primary side
i:	interface
j:	either hot or cold fluid side indication
L:	liquid phase
Lb:	liquid bulk phase
Lf:	liquid film phase
w:	wall (plate)
w/c:	wall / cold fluid boundary
w/h:	wall / hot fluid boundary

Abbreviation

A-C:	absorption column
ACM:	Aspen Custom Modeler®
CSTR:	continuous stirred tank reactor
D-C:	desorption column
DAE:	differential and algebraic equations
HE:	heat exchanger
LRHE:	lean-rich heat exchanger
MEA:	monoethanolamine
PDAE:	partial differential and algebraic equations

Few experimental studies on absorption dynamics were published, but all published data are incomplete. Faber et al. (2011) presented three different experiments on the dynamic closed-loop process behavior, without giving sufficient details on the geometry and periphery. For instance, no information is available for the liquid distributors and HEs installed. It is generally difficult to ensure reproducibility of transient experiments (Wu et al., 2020), which may be one of the main reasons for lacking data. Bui et al. (2016) tried to close this gap and published experimental data obtained from the pilot plant built at Loy Yang power station in Australia. This plant was operated under a broad range of transient conditions (varied flue gas flow rate, liquid absorbent flow rate and steam pressure) to capture the process dynamics. Nevertheless, the information on the liquid distributors and the periphery is

still missing in this paper. Thus, any validation of a dynamic closed-loop model with experimental data is missing.

In this paper, a novel model for the dynamic simulation of the overall closed-loop absorption process is presented. The model was developed and validated against experimental data. The packings installed in the absorption and desorption columns are modeled using the rate-based approach. Reaction kinetics, both in the film and the bulk region, and the influence of the electrolytes were taken into account, because approaches with lower model rigor fail to capture absorption process kinetics (Kenig et al., 2003). Furthermore, our preliminary simulation studies have shown a significant influence of the periphery and non-separating column internals on the overall process dynamics, especially regarding the liquid distributors (Bothe et al., 2021). Since

information on the liquid distributors is neither available for the pilot plant built in Esbjerg, Denmark (Faber et al., 2011) nor for the Australian pilot plant (Bui et al., 2016), we carried out transient experiments at our own pilot plant (Fig. 1) and obtained the validation data for the simulations. This pilot plant has been basically designed as a multi-purpose set-up and experiments can be carried out in different configurations, e.g., with single packed columns or in the closed-loop mode. The latter mode was used in this work. A continuous measurement of liquid-phase and gas-phase compositions was, however, not possible because the plant was designed for investigations of steady-state absorption/desorption operations.

2. Dynamic modeling

The typical absorption plant, as shown in Fig. 1, consists of several components, all being important for dynamic modeling. For these components, different dynamic modeling approaches were used that are listed in Table 1. Their detailed description is given in the next sections.

2.1. Dynamic rate-based approach

Schneider et al. (1999) developed a rate-based dynamic model for the chemical absorption of coke oven gas (see Fig. 2). This model is adapted here for the description of the absorption/desorption processes within the columns internals. Each stage of the columns is described with the two-film theory. The resistance to mass transfer is concentrated in thin films adjacent to the phase interface and the mass transfer occurs within this film by steady-state molecular diffusion. The diffusion and reaction kinetics are directly accounted for in the mass and heat balance equations, while necessary parameters for calculation are determined with correlations obtained from the literature. Furthermore, the specific features of electrolyte solutions are included. In the following, the model equations are presented in a general form.

2.1.1. Bulk phases

For the liquid (solvent) bulk phase, the component material and energy balance equations are formulated as follows:

Table 1
Plant components with corresponding modeling approaches.

Plant component	Dynamic modeling approach	Refs.
Columns:		
• Packing bed	Dynamic rate-based approach	Schneider et al. (1999)
• Liquid distributor	CSTR (cascade) model	Schneider et al. (1999)
• Column bottoms	CSTR model	Schneider et al. (1999)
Heat Exchangers:		
• Plate heat exchanger	Dynamic 1D heat transfer model	Bobić et al. (2020)
• Evaporator	CSTR model	Huepen and Kenig (2010)
Pipelines:		
• Solvent	CSTR cascade model	Westerterp et al. (1984)
• Gas	- Neglected -	

$$\frac{\partial}{\partial t}(U_i^{Lb} x_i^{Lb}) = \frac{\partial}{\partial z}(L^{Lb} x_i^{Lb}) + (n_i^{Lb} a^i + R_i^{Lb} \phi^L)A, \quad i = 1, \dots, NC^L \quad (1)$$

$$\frac{\partial}{\partial t}(U_i^{Lb} \bar{h}^{Lb}) = \frac{\partial}{\partial z}(L^{Lb} \bar{h}^{Lb}) + q^{Lf} a^i A \quad (2)$$

$$\sum_{i=1}^{NC^L} x_i^{Lb} = 1 \quad (3)$$

The volumetric liquid holdup ϕ^L depends on the gas and liquid flow rates and is determined from empirical packing correlations. In this work, the correlation of Billet and Schultes (1999) is used.

For the gas bulk phase, the balance equations look similar, but the specific molar holdup U_i^{Gb} is mostly neglected due to the low gas-phase density, and the component balance equation for the gas phase becomes:

$$0 = -\frac{\partial}{\partial z}(G^{Gb} y_i^{Gb}) - (n_i^{Gb} a^i - R_i^{Gb} \phi^G)A, \quad i = 1, \dots, NC^G \quad (4)$$

$$0 = -\frac{\partial}{\partial z}(G^{Gb} \bar{h}^{Gb}) - q^{Gf} a^i A \quad (5)$$

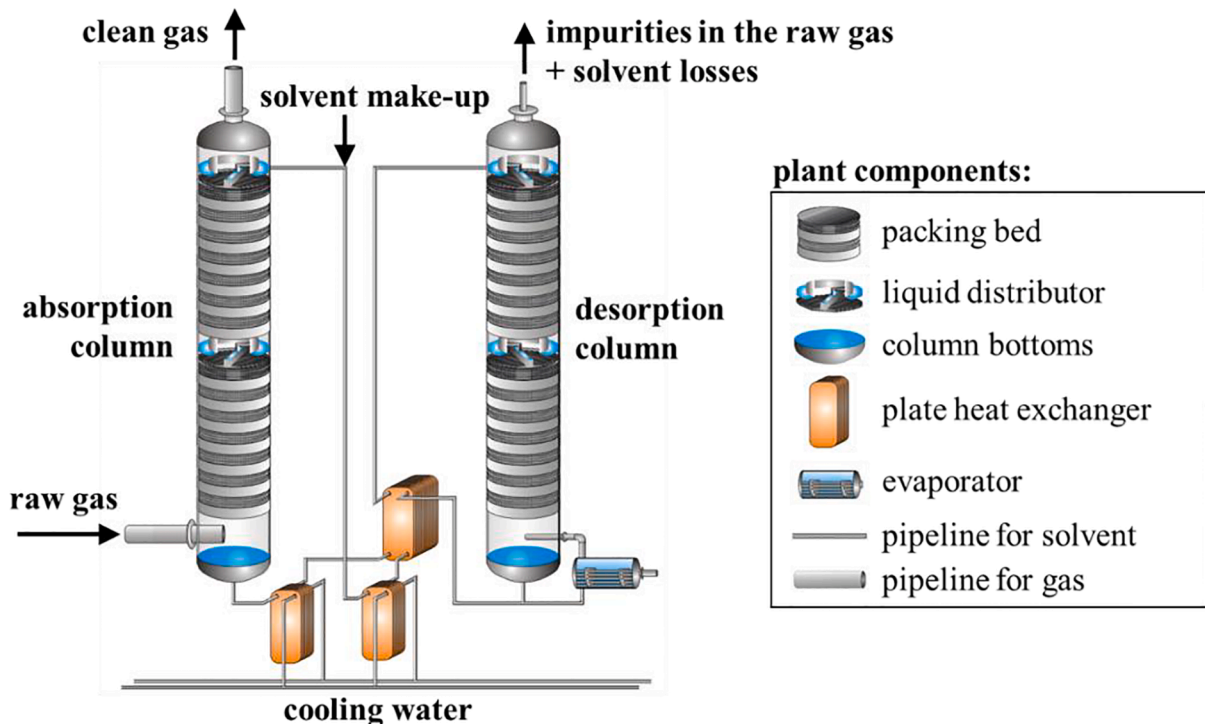


Fig. 1. Simplified flowsheet of the pilot plant at Paderborn University in a closed-loop configuration, adapted from Hüser and Kenig (2014).

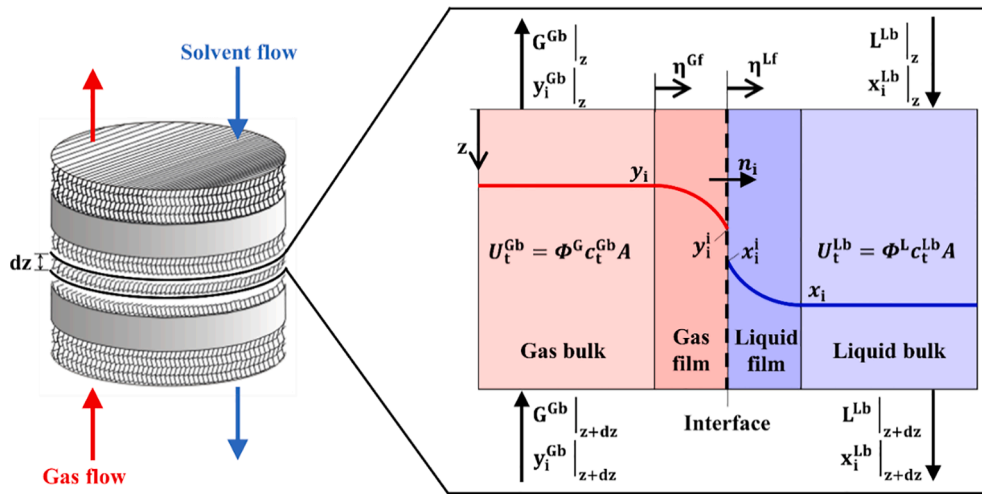


Fig. 2. Schematic of a packing bed (left) and the two-film model representing one stage of this bed (right), adapted from Schneider et al. (1999).

$$\sum_{i=1}^{NC^G} y_i^{Gb} = 1 \quad (6)$$

$$\phi^L + \phi^G = 1 \quad (7)$$

In addition to the volumetric liquid holdup ϕ^L , pressure drop Δp is evaluated using the correlation of Billet and Schultes (1999) and the effective phase interface a^i is estimated by the correlation of Tsai et al. (2011).

2.1.2. Film phases

The transport phenomena within the film are commonly considered as a steady-state problem (Kooijman and Taylor, 1995). The key assumptions of the film model result in the one-dimensional mass transport normal to the interface (η -coordinate), and hence, the differential component balance equations comprising simultaneous mass transfer and reaction have the following form:

$$0 = -\frac{1}{\delta^L} \frac{\partial n_i^{Lf}}{\partial \eta^{Lf}} + R_i^{Lf}, \quad i = 1, \dots, NC^L \quad (8)$$

$$0 = -\frac{1}{\delta^G} \frac{\partial n_i^{Gf}}{\partial \eta^{Gf}} + R_i^{Gf}, \quad i = 1, \dots, NC^G \quad (9)$$

In dilute electrolyte systems, component fluxes n_i can be determined with the Nernst-Planck equation (Taylor and Krishna, 1993):

$$n_i^{Lf} = -\frac{c_i^{Lf} D_{i,eff}^{Lf}}{\delta^L} \left(\frac{\partial x_i^{Lf}}{\partial \eta^{Lf}} + x_i^{Lf} z_i \frac{F}{RT} \frac{\partial \varphi}{\partial \eta^{Lf}} \right) + x_i^{Lf} n_i^{Lf}, \quad i = 1, \dots, NC^L \quad (10)$$

The inclusion of the electrical potential requires an additional condition of the electroneutrality to be fulfilled in the liquid phase:

$$\sum_{i=1}^{NC^L} x_i z_i = 0 \quad (11)$$

In the gas-film region, the component fluxes are described by:

$$n_i^{Gf} = -\frac{c_i^{Gf} D_{i,eff}^{Gf}}{\delta^G} \frac{\partial y_i^{Gf}}{\partial \eta^{Gf}} + y_i^{Gf} n_i^{Gf}, \quad i = 1, \dots, NC^G \quad (12)$$

The boundary conditions for the liquid and gas film are as follows:

$$x_i^{Lf}(\eta^{Lf} = 0) = x_i^i, \quad x_i^{Lf}(\eta^{Lf} = 1) = x_i^{Lb}, \quad i = 1, \dots, NC^L \quad (13)$$

$$y_i^{Gf}(\eta^{Gf} = 0) = y_i^{Gb}, \quad y_i^{Gf}(\eta^{Gf} = 1) = y_i^i, \quad i = 1, \dots, NC^G \quad (14)$$

The heat fluxes in the film regions are given by:

$$q^{Lf} = -\frac{\lambda^L}{\delta^L} \frac{\partial T^L}{\partial \eta^{Lf}} + \sum_{i=1}^{NC^L} n_i^{Lf} \bar{h}^{Lf} \quad (15)$$

$$q^{Gf} = -\frac{\lambda^G}{\delta^G} \frac{\partial T^G}{\partial \eta^{Gf}} + \sum_{i=1}^{NC^G} n_i^{Gf} \bar{h}^{Gf} \quad (16)$$

The film thicknesses δ^L and δ^G are estimated via mass transfer coefficients (Taylor and Krishna, 1993). The coefficients are determined using the empirical correlations from Billet and Schultes (1999).

2.1.3. Interface

At the phase interface, thermodynamic equilibrium is assumed. The corresponding equations are used to connect the gas and liquid phase compositions:

$$y_i^i = K_i x_i^i, \quad i = 1, \dots, NC^G \quad (17)$$

Furthermore, the component flux continuity must be fulfilled at the phase interface:

$$n_i^{Gf}(\eta^{Gf} = 1) = n_i^{Lf}(\eta^{Lf} = 0), \quad i = 1, \dots, NC^G \quad (18)$$

2.2. Dynamic 1D heat transfer model

In the left-hand part of Fig. 3, a schematic of an ideal counterflow plate HE is shown. The entering fluid flows are distributed among all channels, separated by corrugated plates. The hot and cold fluids flow alternately through the channels along the z -coordinate. The temperature difference between the hot and cold fluid leads to heat transport through the plate. The superscripts h and c denote the hot fluid and cold fluid, correspondingly.

Bobić et al. (2020) proposed a dynamic model for ideal counterflow plate HES. In order to take the changes of fluid temperature in z -direction into account, each channel is subdivided into several stages with the height Δz . A stage numbered with index n and including one plate is shown in the right-hand part of Fig. 3. The key assumptions of the heat transfer model by Bobić et al. (2020) results in the one-dimensional heat transport normal to the interface (x -coordinate). The assumptions include a uniform temperature over the fluid flow channel width (y -direction), single-phase fluids, no heat transfer into the environment due to isolation and no heat conduction in z -direction in the fluids and the plate. We used this approach for the plate HES in our dynamic closed-loop model. Accordingly, the material and energy balance equations of the hot and cold fluid, considering convective heat transfer between the fluid and the adjacent plate, have the following form:

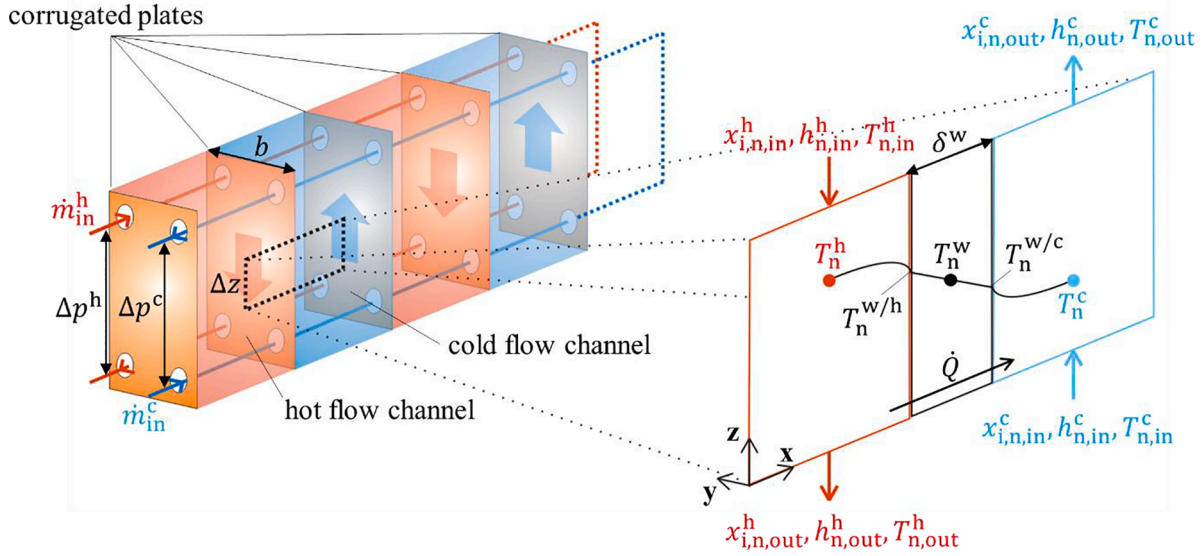


Fig. 3. Schematic of an ideal counterflow plate HE (left) with enlarged illustration of a single stage (right).

$$\dot{m}_{n,in}^j = \dot{m}_{n,out}^j = \dot{m}^j, \quad j \in \{h, c\} \quad (19)$$

$$V_{n,c,p,n}^j \rho_n^j \frac{dT_n^j}{dt} = \dot{m}^j c_{p,n}^j (T_{n,in}^j - T_{n,out}^j) + A_n \alpha_n^j (T_n^{w/j} - T_n^j), \quad j \in \{h, c\} \quad (20)$$

where α is the heat transfer coefficient and $A_n = b\Delta z$ the heat exchange area. The superscripts w/h and w/c refer to the temperatures on the boundaries between the wall (plate) and the hot and cold fluid, respectively.

Bobić et al. (2020) validated their model using experiments with pure water, both as a hot and a cold fluid. Thus, no reaction terms were considered in the mass and heat balance equations. In contrast, our model should be applicable to multicomponent liquids in which reactions take place. Due to the reactions, the liquid composition changes between inlet and outlet. This can be considered using the following equation:

$$V_{n,c,n,t}^j \frac{dx_{i,n,out}^j}{dt} = L_{n,in}^j x_{i,n,in}^j - L_{n,out}^j x_{i,n,out}^j + R_i^j V_n^j, \quad (21)$$

$$i = 1, \dots, NC^L, \quad j \in \{h, c\}$$

The heat of reaction is considered implicitly, using the inlet and outlet fluid enthalpies, and therefore, Eq. (20) obtains the following form:

$$V_{n,c,n,t}^j \frac{dH_{n,out}^j}{dt} = L_{n,in}^j H_{n,in}^j - L_{n,out}^j H_{n,out}^j + A_n \alpha_n^j (T_n^{w/j} - T_n^j), \quad j \in \{h, c\} \quad (22)$$

As shown in the work of Michel and Kugi (2014), the conductive heat transfer through the plate in the x -direction can be considered in a simplified manner due to the small plate thickness δ^w of the HE and the large thermal conductivity λ^w of the plate material. This holds for most plate HEs. The conductive heat transfer through the wall is modeled based on the average wall temperature T_n^w determined in the middle (cf. Fig. 3). The corresponding energy balance equation in stage n can be written as:

$$V_n^w \rho^w c_p^w \frac{dT_n^w}{dt} = A_n \frac{2\lambda^w}{\delta^w} [(T_n^{w/h} - T_n^w) - (T_n^w - T_n^{w/c})] \quad (23)$$

In order to model the thermal coupling between the two fluids and the wall, considering the assumption of quasi-steady heat transfer in x -direction as shown in Fig. 3 on the right side, the temperatures $T_n^{w/h}$ and $T_n^{w/c}$ must be expressed as:

$$T_n^{w/j} = T_n^j - \frac{k_n^j}{\alpha_n^j} (T_n^j - T_n^w), \quad j \in \{h, c\} \quad (24)$$

where the corresponding heat transfer coefficients of the hot and cold side are given with the following relation:

$$\frac{1}{k_n^j} = \frac{1}{\alpha_n^j} + \frac{\delta^w}{2\lambda^w}, \quad j \in \{h, c\} \quad (25)$$

The heat transfer coefficient α_n^j depends on the thermal conductivity of the fluid λ , the Nusselt number Nu and the hydraulic diameter d_h as:

$$\alpha_n^j = \frac{\lambda_n^j}{d_h} Nu_n^j, \quad j \in \{h, c\} \quad (26)$$

The correlation for the Nusselt number depends on the shape of the plates. In case of corrugated plates, the correlation of Martin et al. (2019) is recommended.

2.2.1. Types of plate HE

Industrial plate HEs usually consist of about 100 plates, with alternate flow of hot and cold fluids between them. Thereby, a counterflow, a co-current flow and combinations of both are possible. In Fig. 4a and b, two examples of different plate HEs with $N_{plate} = 9$, resulting in 8 channels for the fluid flows, are given. In order to distinguish the differences between the HEs shown in Fig. 4, the following definitions are used according to Martin et al. (2019):

- Channel (ch): A channel is the space between two plates.
- Passage (pg): A passage is an arbitrary number of channels in which the fluid (hot or cold) flows in parallel (in z -direction).
- Side: A side refers to the entirety of all channels through which the same fluid flows. Each plate HE consists of two sides (hot fluid side/cold fluid side).

Consequently, various types of plate HEs can be described using the following nomenclature: $(pg_1 \times ch_1 / pg_2 \times ch_2)$, while ch_1 is the number of parallel hot flow channels that pass the HE pg_1 times, and a similar nomenclature applies to the second side. Thus, Fig. 4a shows a $(1 \times 4 / 1 \times 4)$ plate HE (ideal counterflow), while Fig. 4b depicts a $(2 \times 2 / 2 \times 2)$ plate HE. The $(2 \times 2 / 2 \times 2)$ plate HE consists on each side of a series connection of two passages, with two parallel channels each.

In Fig. 5, the discretization of the $(2 \times 2 / 2 \times 2)$ plate HE with fluid

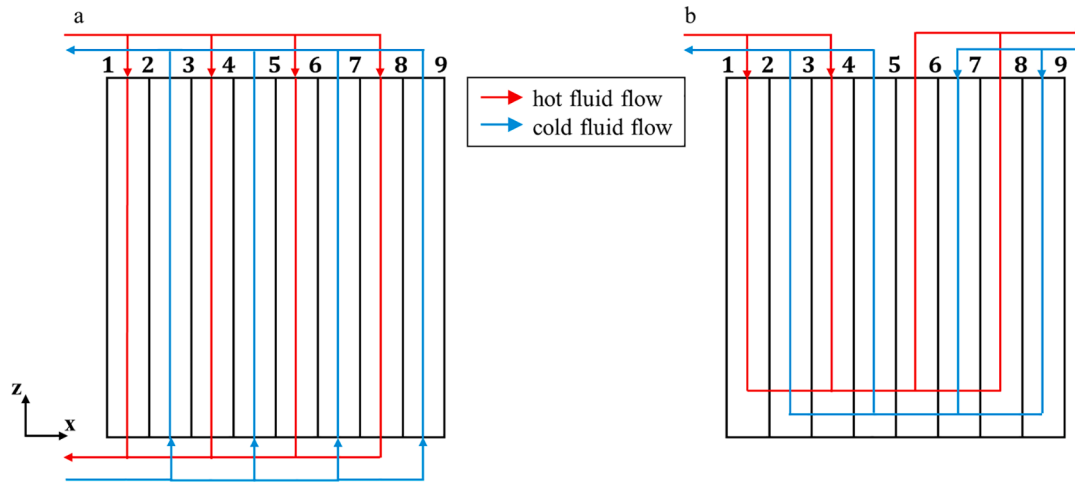


Fig. 4. Schematic of a (1 × 4/1 × 4) plate HE (a) and a (2 × 2/2 × 2) plate HE (b).

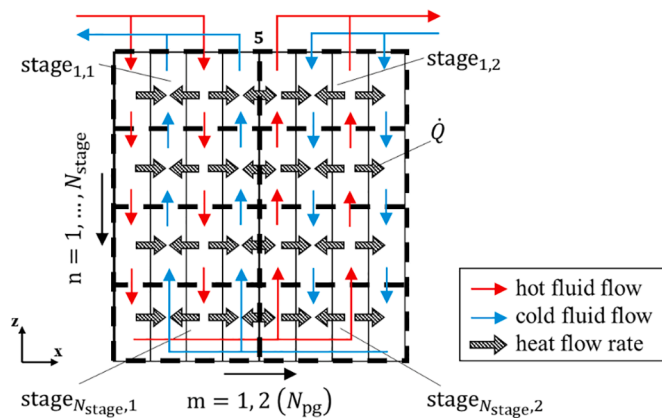


Fig. 5. Discretization of the (2 × 2/2 × 2) plate HE.

and heat flow directions is illustrated. In order to model different types of plate HEs with different flow patterns, the 1D heat transfer model, presented in Section 2.2, would have to be used to calculate every single heat flow rate \dot{Q} (shown with crosshatched arrows in Fig. 5) separately. This will result in a very high number of equations to be solved when simulating plate HEs consisting of about 100 plates. In order to reduce the computational effort, the heat flow rates \dot{Q} can be estimated per passage rather than per plate. This is realized with the HE discretization shown by the dashed black lines in Fig. 5. Within each of the resulting stages, the 1D heat transfer model is applied. In order to calculate the heat flow rate per stage, the heat exchange area of all plates $N_{plate,n}$ as well as the total volume and hydraulic diameters of all channels $N_{ch,n}$ inside the stage must be determined. For the case that both sides have the same number of channels, we obtain:

$$N_{plate,n} = \frac{N_{plate} - 1 - N_{pg}}{N_{pg}}, \quad N_{ch,n} = \frac{N_{plate} - 1}{2 \cdot N_{pg}} \quad (27)$$

Assuming that the fluid flow rate in z -direction in all hot channels is the same and that this is true for all cold channels, the total heat exchange area, total volume and hydraulic diameter of the stage can be determined by:

$$\begin{aligned} A_n &= N_{plate,n} b \Delta z, & V_n^j &= N_{ch,n} V_{ch}^j, & V_n^w &= A_n \delta^w, \\ d_h^j &= N_{ch,n} d_{h, ch}^j, & j &\in \{h, c\} \end{aligned} \quad (28)$$

resulting in three average temperatures for the hot fluids T_n^h , cold fluids T_n^c , and the plates T_n^w in each stage.

For plate HEs with $N_{pg} > 1$, the ideal counterflow is disturbed through the turn of the flow direction inside the HE. In the example shown in Fig. 5, the fluids along the 5th plate flow co-currently. It is also possible that the temperature of the cold side is already higher than the temperature of the hot side, so that the heat flow rate through the 5th plate is reversed (from the cold side to the hot side), resulting in lower efficiency of the plate HE. However, the lower effectiveness must be accepted if the ideal counterflow plate HEs cannot be installed in the plant due to the design. In order to model the thermal coupling between the hot and cold side through the 5th plate, Eq. (23) for a single plate is used.

2.3. CSTR model

The CSTR (continuous stirred tank reactor) model is typically used to describe the fluid dynamic behavior of a liquid-phase flow with defined holdup; it is applied for various plant components in this work (see Table 1). The CSTR is a batch reactor with ideal mixing conditions, shown in Fig. 6a.

The amount of CSTR residuals is significant, which leads to an additional conversion in the case of chemical reactions and influences the process dynamics. The corresponding material and energy balance equations are as follows:

$$\frac{d(V C_i x_{i,out})}{dt} = L_{in} x_{i,in} - L_{out} x_{i,out} + R_i V, \quad i = 1, \dots, NC^L \quad (29)$$

$$\frac{d(V C_i h_{out})}{dt} = L_{in} h_{in} - L_{out} h_{out} \pm \dot{Q} \quad (30)$$

where changes of the CSTR residuals V are taken into account.

In the case of an evaporator, the heat supply \dot{Q} is added in Eq. (30). It leads to partial evaporation of the liquid. Assuming thermodynamic equilibrium, the vapor composition can be determined by equilibrium relationships. The gas holdup is neglected due to the low gas-phase density. By using the enthalpy in the energy balance equation, the phase change enthalpy and reaction enthalpy are directly taken into account. All chemical reactions in the solvent can be considered as instantaneous due to the high temperatures in the evaporator (Huepen and Kenig, 2010).

Fluid flow in a single CSTR tends to strong backmixing. The fluid particles do not necessarily move through the CSTR with the same velocity, resulting in a broad residence time distribution. This is a common behavior of plant elements in which the liquid movement is slow, e.g., in the column bottoms (Schneider et al., 1999). For plant elements with high fluid velocities, e.g., in the pipeline, narrow residence time

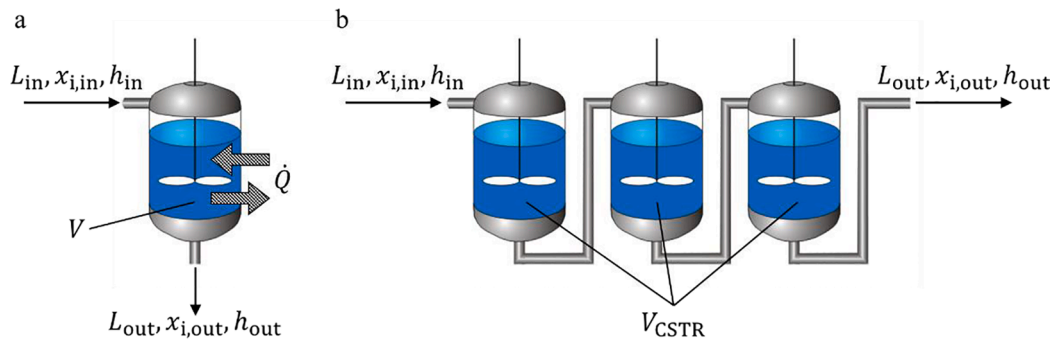


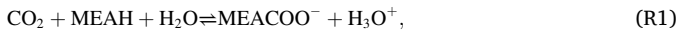
Fig. 6. Schematic of a single CSTR (a) and a cascade of three CSTRs (b).

distributions can be encountered. This can be modeled with a CSTR cascade shown in Fig. 6b (Westerterp et al., 1984). The total volume of the CSTR residuals is split into several parts: $V = N_{CSTR} \cdot V_{CSTR}$. The higher the number of CSTR N_{CSTR} is, the narrower residence time distribution is obtained. In an ideal flow tube reactor, it corresponds to a step response ($N_{CSTR} \rightarrow \infty$). For modeling the dynamics of a real pipeline, $N_{CSTR} = 3$ is usually sufficient (Westerterp et al., 1984).

For the dynamic modeling of the liquid distributors and column bottoms, the single CSTR model without a source term in Eq. (30) is used and interactions with the surrounding gas phase are excluded (Schneider et al., 1999).

2.4. Chemical reaction system

The proposed dynamic model is applied in our work to describe the carbon dioxide (CO_2) capturing by aqueous monoethanolamine (MEA) solution; however, it can be extended to cover further chemical systems and applications. The overall reaction system governing the absorption of CO_2 with MEA involves a complex set of parallel and consecutive reactions in the liquid phase (Kucka et al., 2003). Two of them are kinetically controlled reversible reactions:



whereas three other reactions are instantaneous reversible:



The implementation of the reactions is realized using the species reaction rate R_i in Eqs. (1), (8), (21) and (29). All reactions take place in the liquid phase, and hence, $R_i^{\text{gb}} = R_i^{\text{gf}} = 0$. The R_i values are determined from the equivalent reaction rate r_i and the stoichiometric coefficients $\nu_{i,r}$ of the corresponding reaction r :

$$R_i = \sum_{r=1}^{R5} (\nu_{i,r} r_i), \quad i = 1, \dots, NC^L \quad (31)$$

For kinetically controlled reversible reactions, the equivalent

reaction rate r_i is obtained by:

$$r_i = k_{r,\text{for}} \prod_c (x_c \gamma_c)^{\nu_{c,r}} - k_{r,\text{back}} \prod_p (x_p \gamma_p)^{\nu_{p,r}} \quad (32)$$

while instantaneous reversible reactions are described by the law of mass action as follows:

$$K_r = \frac{\prod_p (x_p \gamma_p)^{\nu_{p,r}}}{\prod_c (x_c \gamma_c)^{\nu_{c,r}}} \quad (33)$$

The reaction rate constants k_r in Eq. (32) and the equilibrium constants K_r in Eq. (33) are estimated via empirical correlations from literature that are given in Table 2 and Table 3.

3. Experiments

For the validation, we performed two experiments to monitor the dynamic process behavior of the pilot plant shown in Fig. 1. The plant data is given in Table 4. The operating (absolute) pressure in the absorption column is 1 bar; in the desorption column, it is at slightly increased value of 1.1 bar. Further operating conditions for the experiments are given in Table 5. The humidity in the gas phase is calculated using the Antoine equation. The heat supply in the evaporator could not be directly measured. Therefore, it was adjusted to the outlet solvent temperature of the desorption column. The liquid CO_2 concentration was not measured.

For the experimental investigation of the dynamic process behavior, the solvent mass flow rate is reduced from 150 to 100 kg/h. As soon as the changes in the outlet CO_2 gas-phase concentration and temperatures become insignificant, the mass flow rate is set back to 150 kg/h. All other operating conditions are kept constant. The transient process behavior was measured for a total time of about 1.5 h. The corresponding simulation time took 20–30 h for one dynamic simulation of the overall closed-loop process (without the simulation time of the initial steady-state). The computer used was AMD Phenom™ X4 955 processor, RAM: 16.00 GB.

4. Results

The developed dynamic model was implemented into the commercial software tool Aspen Custom Modeler® (ACM). The model comprises a system of partial differential and algebraic equations (PDAE). A dis-

Table 2
Correlations used in this paper for the determination of the reaction rate k_r .

Reaction	$k_{r,\text{for}}$	$k_{r,\text{back}}$	Reference
R1	$1.33 \cdot 10^{17} \exp\left(-\frac{55470.91}{RT}\right)$	$3.02 \cdot 10^{14} \exp\left(-\frac{41264.26}{RT}\right)$	Pinsent et al. (1956)
R2	$6.63 \cdot 10^{16} \exp\left(-\frac{107416.54}{RT}\right)$	$5.52 \cdot 10^{23} \exp\left(-\frac{69157.56}{RT}\right)$	Hikita et al. (1977)

Table 3

Correlations used in this paper for the determination of the equilibrium constant: $\ln K_r = a + \frac{b}{T} + cT + d \ln T$.

Reaction	a	b	c	d	Reference
R3	0.7996	- 8094.81	0.0	- 0.007484	Austgen et al. (1989)
R4	216.049	- 12431.7	- 35.4819	0.0	Austgen et al. (1989)
R5	132.899	- 13445.9	- 22.4773	0.0	Austgen et al. (1989)

cretization with respect to the axial z -coordinate and normal η -coordinate has been carried out, resulting in a differential and algebraic equations system (DAE). Grid independence studies were carried out to determine the number of axial stages and film elements in the column model as well as the number of stages in the 1D heat transfer model for the plate HEs. These numbers were gradually increased until the simulation results showed no significant changes. In order to check whether this state is reached, one parameter obtained from the simulation results was monitored as a function of the number of stages. For the absorption resp. desorption column, grid independence was controlled with the absorption (desorption) efficiency determined as follows:

$$\Psi = \left(\frac{G_{in,yCO_2,in} - G_{out,yCO_2,out}}{G_{in,yCO_2,out}} \right) \cdot 100\% \quad (34)$$

It is the most important parameter for evaluating the absorption/desorption performance. For the plate HEs, the outlet temperature of the hot fluid was chosen to check grid independence. The physical properties are determined with the Aspen Properties database as a function of temperature, pressure and composition.

The simulated and experimental results for the first experiment are shown in Fig. 7. In Fig. 7a, the inlet gas and solvent mass flow rates are depicted that illustrate the changes performed. The first change in solvent mass flow rate from 150 to 100 kg/h was made at 0.18 h and is shown with a vertical dashed line (black) in Fig. 7. The second vertical dashed line (black) at 0.79 h represents the change back to 150 kg/h. In Figs. 7b and c, the inlet and outlet temperatures in the desorption and absorption column are shown. Due to the reduced solvent mass flow rate, the constant heat supply in the evaporator leads to higher temperatures of the solvent leaving the desorption column (Fig. 7b). Due to the larger diameter of the desorption column (see Table 4), its holdup is large resulting in a longer transition behavior. After passing the HEs, the solvent with higher temperature leaving the desorption column is cooled down and enters the absorption column (Fig. 7c). The measured inlet solvent temperature of the absorption column decreases after the reduction in mass flow rate from 150 to 100 kg/h, whereas no significant

Table 4

Pilot plant data.

	Amount [-]	Length [m]	Diameter [m]	Area [m x m]	Material
Absorption column (A-C):					
Packing bed	2	1.5	0.1	-	Mellapak 250Y
Distributor	2	0.06	0.1	-	-
Column bottoms	1	0.09	0.1	-	-
Desorption column (D-C):					
Packing bed	2	1.5	0.3	-	Mellapak 250Y
Distributor	2	0.02	0.3	-	-
Column bottoms	1	0.17	0.3	-	-
Plate HE:					
(2 × 5 / 2 × 5)	2	0.475	-	0.115 × 0.063	Nickel
(1 × 39 / 1 × 40)	1	0.475	-	0.115 × 0.292	Nickel
(LRHE)					
Evaporator	1	0.68	0.1594	-	-
Pipeline for solvent from:					
A-C to LRHE	1	3.0	0.02	-	Stainless steel
LRHE to D-C	1	7.0	0.02	-	Stainless steel
D-C to LRHE	1	3.0	0.02	-	Stainless steel
LRHE to A-C	1	7.0	0.02	-	Stainless steel

change of the simulated inlet temperature can be observed. In addition to the evaporator heat supply, the solvent is heated by the reactions taking place in the absorption column. The simulated outlet temperatures of the absorption column shown in Fig. 7c are slightly lower than the measured values but show the same qualitative course. Fig. 7b shows peaks in the measured inlet solvent temperature of the desorption column after the change in solvent mass flow rate, especially after the change back to 150 kg/h, which the simulation cannot reproduce. Nevertheless, qualitative agreement between the simulated and measured process dynamics is obvious and the outlet temperatures in the solvent and gas phases are well captured by the simulations.

In Fig. 7d, the gas-phase CO₂ concentrations at the absorption column outlet are given. Due to the reduced solvent amount after the first change, the outlet CO₂ gas concentration increases. Along with the full dynamic model, the simulations were carried out with the reduced model that does not include the dynamic behavior of liquid distributors, column bottoms and periphery (state-of-the-art model). The deviation between the measured and simulated CO₂ concentration, obtained with the full dynamic model, is determined by

$$e = \left(\frac{y_{CO_2,exp.} - y_{CO_2,sim.}}{y_{CO_2,exp.}} \right) \cdot 100\% \quad (35)$$

and shown in Fig. 7d. Within the full simulation time, the deviation of the full dynamic model remains below 5%, which is a very good

Table 5

Conditions and compositions of the gas and solvent entering the absorption column.

	First experiment		Second experiment	
	Raw gas	Solvent	Raw gas	Solvent
Mass flow rate [kg/h]	40.2	150 (100)	41.9	150 (100)
Temperature [K]	295.45	288.65	294.65	288.35
MEA concentration [wt.-%]	0	25.32	0	24.97
CO ₂ concentration [vol.-%]	7.28	-	6.55	-

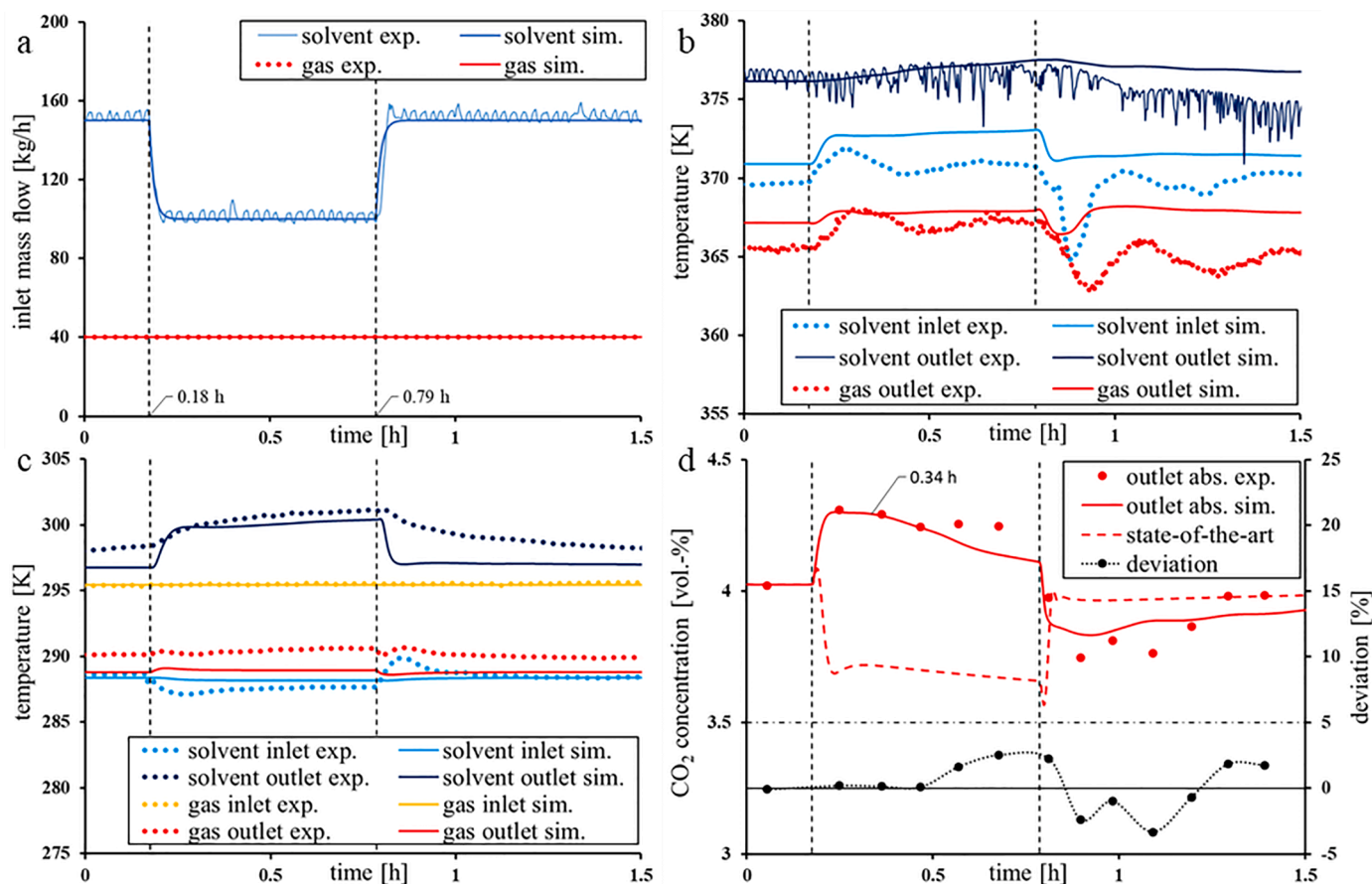


Fig. 7. Results for the first experiment: inlet mass flow rates (a); temperatures in the desorption column (b) and in the absorption column (c); outlet CO₂ gas-phase concentrations with the deviation of the full dynamic model (d).

agreement. The strong influence of the additional holdups in the closed-loop process is obvious, and thus, it is necessary to consider this influence in order to achieve a good agreement between the measurements and simulations. Taking only the holdup in the packings into account results in a large discrepancy and, in essence, in a completely different simulated transient behavior after changing the solvent mass flow rate than in reality. As it is seen in Fig. 7d, the outlet CO₂ gas concentration increases only for few seconds and then drops significantly. This can be explained by the reduced loading of the solvent entering the absorption column due to the higher temperature of the solvent in the evaporator. The solvent with the lower loading enters the absorption column and is capable of capturing more CO₂ thus improving absorption. This influence of the lower loading of the solvent entering the absorption column on the process can be seen in the full dynamic model after some time necessary for the solvent to pass the desorption column, evaporator and the periphery between the desorption and the absorption column. In Fig. 7d, the time, at which the outlet CO₂ gas concentration starts decreasing, can be identified at 0.34 h.

In Fig. 8, the results for the second experiment are shown. They are largely comparable with those of the first experiment, and the strong influence of the liquid distributors and the periphery on the dynamic process behavior can be clearly seen. Due to the slightly lower inlet CO₂ gas-phase concentration (cf. Table 5), also the outlet CO₂ concentrations in Fig. 8d are lower than in the first experiment. In contrast to the first experiment, the simulated initial steady-state deviates from the measurement by 5%. Furthermore, the deviations following the change in mass flow rate are slightly higher here, especially after the first change in mass flow rate. The increase of the outlet CO₂ gas concentration, due to the reduced solvent mass flow rate, is in the measurement much higher than in the simulation. The deviations here are in the range of 5 –

8%, yet still sufficiently low.

In Fig. 8b and c, qualitative courses of the inlet and outlet temperatures similar to those of the first experiment can be seen. However, the peak in the measured inlet solvent temperature of the desorption column after the second change is higher. The peaks are probably encountered due to the pumps that move the loaded solvent to the desorption column and whose dynamic behavior is not considered in the model. Nevertheless, the good agreement between the simulation and measurement results is confirmed with the second experiment, too.

5. Conclusions

In this work, a novel dynamic model of the overall closed-loop absorption/desorption process including the periphery as well as non-separating column internals of the pilot plant was developed and validated against experimental data obtained in the pilot plant at Paderborn University. The chemical absorption of CO₂ with aqueous MEA solutions was used as an example system. The solvent mass flow rate was changed to generate dynamic system responses. Two experiments were carried out. Despite the high complexity of the dynamic model, both the outlet gas-phase concentration and the inlet and outlet temperatures in the columns could be well captured. The deviation between experimental and simulated outlet gas concentrations obtained with the full dynamic model is below 5% for the first experiment and below 10% for the second experiment. The validation performed in this work is a first comprehensive, transparent check of a dynamic closed-loop model for chemical absorption of CO₂ with MEA using full set of experimental data. A strong influence of the column internals and the periphery on the dynamic process behavior is demonstrated.

The model was developed in a general form to be applicable to

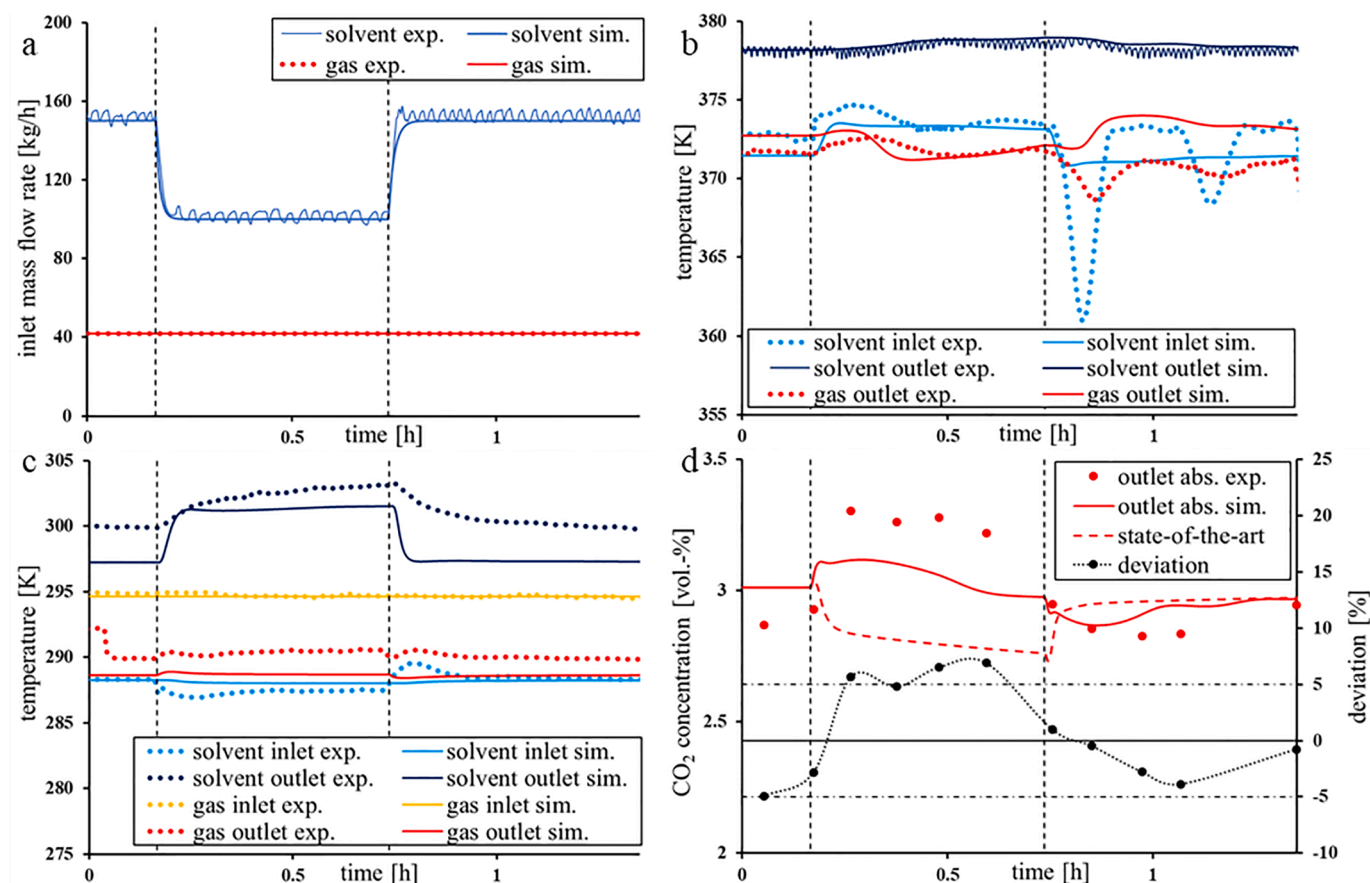


Fig. 8. Results for the second experiment: inlet mass flow rates (a); temperatures in the desorption column (b) and in the absorption column (c); outlet CO₂ gas-phase concentrations with deviation of the full dynamic model (d).

different chemical absorption systems. In this way, systems containing toxic or carcinogenic gas components can also be investigated, which helps to prevent hazardous situations through leaking into the environment. With the suggested model, dynamic simulations can be performed for any changes (disturbances) in the plant yielding information which is difficult to obtain experimentally. For instance, causes for hazardous situations and ways to their possible elimination can be investigated and the duration between a malfunction and the relevant system reaction can be determined. This knowledge of the dynamic process behavior will help to enhance safety of industrial absorption plants. The functional properties of measurement and control devices can be evaluated with respect to their ability to ensure a regular process operation in case of malfunctions. Should not this be possible, additional control strategies can be proposed based on the simulation results.

In the future work, the validated model will be used to analyze the dynamics of the chemical absorption of coke oven gas in response to various plant disturbances. The coke oven gas contains toxic components, such as hydrogen sulfide or ammonia, which represent a great hazard when leaking into the environment. Simulation studies of the various plant disturbances should help to develop efficient strategies preventing hazardous situations.

CRedit authorship contribution statement

Mike Bothe: Conceptualization, Methodology, Software, Validation, Writing – original draft. **Iman Hami Dindar:** Investigation. **Nicole Lutters:** Writing – review & editing. **Eugeniy Y. Kenig:** Conceptualization, Writing – review & editing, Supervision.

Declaration of Competing Interest

The authors declare that they have no known competing financial interests or personal relationships that could have appeared to influence the work reported in this paper.

Data Availability

No data was used for the research described in the article.

References

- Åkesson, J., Laird, C.D., Lavedan, G., Pröhl, K., Tummescheit, H., Velut, S., Zhu, Y., 2012. Nonlinear model predictive control of a CO₂ post-combustion absorption unit. *Chem. Eng. Technol.* 35 (3), 445–454. <https://doi.org/10.1002/ceat.201100480>.
- Austgen, D.M., Rochelle, G.T., Peng, X., Chen, C.C., 1989. Model of vapor-liquid equilibria for aqueous acid gas-alkanolamine systems using electrolyte NRTL equation. *Ind. Eng. Chem. Res.* 28 (7), 1060–1073. <https://doi.org/10.1021/ie00091a028>.
- Billet, R., Schultes, M., 1999. Prediction of mass transfer columns with dumped and arranged packings: updated summary of the calculation method of Billet and Schultes. *Chem. Eng. Res. Des.* 77 (6), 498–504. <https://doi.org/10.1205/026387699526520>.
- Biliyok, C., Lawal, A., Wang, M., Seibert, F., 2012. Dynamic modelling, validation and analysis of post-combustion chemical absorption CO₂ capture plant. *Int. J. Greenh. Gas Control* 9, 428–445. <https://doi.org/10.1016/j.ijggc.2012.05.001>.
- Bobić, M., Gjerek, B., Golobič, I., Bajsić, I., 2020. Dynamic behaviour of a plate heat exchanger: influence of temperature disturbances and flow configurations. *Int. J. Heat Mass Transf.* 163, e120439 <https://doi.org/10.1016/j.ijheatmasstransfer.2020.120439>.
- Bothe, M., Lutters, N., Kenig, E.Y., 2021. Examination of hazardous situations in industrial closed-loop processes using dynamic simulations. *Chem. Eng. Trans.* 88, 703–708. <https://doi.org/10.3303/CET2188117>.
- Bui, M., Gunawan, I., Verheyen, V., Feron, P., Meuleman, E., 2016. Flexible operation of CSIRO's post-combustion CO₂ capture pilot plant at the AGL Loy Yang power station.

- Int. J. Greenh. Gas Control 48, 188–203. <https://doi.org/10.1016/j.ijggc.2015.12.016>.
- Dugas, R.E., 2006. Pilot plant study of carbon dioxide capture by aqueous monoethanolamine. The University of Texas at Austin, USA (MSc thesis).
- Faber, R., Köpcke, M., Biede, O., Knudsen, J.N., Andersen, J., 2011. Open-loop step responses for the MEA post-combustion capture process: Experimental results from the Esbjerg pilot plant. Energy Procedia 4, 1427–1434. <https://doi.org/10.1016/j.egypro.2011.02.008>.
- Gáspár, J., Cormos, A.-M., 2011. Dynamic modeling and validation of absorber and desorber columns for post-combustion CO₂ capture. Comput. Chem. Eng. 35 (10), 2044–2052. <https://doi.org/10.1016/j.compchemeng.2010.10.001>.
- Kenig, E.Y., Kucka, L., Górák, A., 2003. Rigorous modeling of reactive absorption processes. Chem. Eng. Technol. 26 (6), 631–646. <https://doi.org/10.1002/ceat.200390096>.
- Kooijman, H.A., Taylor, R., 1995. A nonequilibrium model for dynamic simulation of tray distillation columns. AIChE J. 41 (8), 1852–1863. <https://doi.org/10.1002/aic.690410804>.
- Kucka, L., Müller, I., Kenig, E.Y., Górák, A., 2003. On the modelling and simulation of sour gas absorption by aqueous amine solutions. Chem. Eng. Sci. 58 (16), 3571–3578. [https://doi.org/10.1016/S0009-2509\(03\)00255-0](https://doi.org/10.1016/S0009-2509(03)00255-0).
- Kvamsdal, H.M., Jakobsen, J.P., Hoff, K.A., 2009. Dynamic modeling and simulation of a CO₂ absorber column for post-combustion CO₂ capture. Chem. Eng. Process. 48, 135–144. <https://doi.org/10.1016/j.cep.2008.03.002>.
- Harun, N., Nittaya, T., Douglas, P.L., Croiset, E., Ricardez-Sandoval, L.A., 2012. Dynamic simulation of MEA absorption process for CO₂ capture from power plants. Int. J. Greenh. Gas Control 10, 295–309. <https://doi.org/10.1016/j.ijggc.2012.06.017>.
- Hikita, H., Asai, S., Ishikawa, H., Honda, M., 1977. The kinetics of reactions of carbon dioxide with monoethanolamine, diethanolamine and triethanolamine by a rapid mixing method. Chem. Eng. J. 13 (1), 7–12. [https://doi.org/10.1016/0300-9467\(77\)80002-6](https://doi.org/10.1016/0300-9467(77)80002-6).
- Huepen, B., Kenig, E.Y., 2010. Rigorous modeling and simulation of an absorption–stripping loop for the removal of acid gases. Ind. Eng. Chem. Res. 49 (2), 772–779. <https://doi.org/10.1021/ie9003927>.
- Hüser, N., Kenig, E.Y., 2014. A new absorption-desorption pilot plant for CO₂ capture. Chem. Eng. Trans. 39, 1417–1422. <https://doi.org/10.3303/CET1439237>.
- Martin, H., Dietrich, B., Nickolay, M., 2019. Druckverlust und Wärmeübergang in Plattenwärmeübertragern: VDI-Wärmeatlas. Springer, Berlin, pp. 1687–1697.
- Michel, A., Kugi, A., 2014. Model based control of compact heat exchangers independent of the heat transfer behavior. J. Process Control 24 (4), 286–298. <https://doi.org/10.1016/j.jprocont.2014.02.003>.
- Pinsent, B.R.W., Pearson, L., Roughton, F.J.W., 1956. The kinetics of combination of carbon dioxide with hydroxide ions. Trans. Faraday Soc. 52, 1512–1520. <https://doi.org/10.1039/TF9565201512>.
- Schneider, R., Kenig, E.Y., Górák, A., 1999. Rigorous dynamic modelling of complex reactive absorption processes. Chem. Eng. Sci. 54 (21), 5195–5203. [https://doi.org/10.1016/S0009-2509\(99\)00240-7](https://doi.org/10.1016/S0009-2509(99)00240-7).
- Taylor, R., Krishna, R., 1993. Multicomponent mass transfer. Wiley, New York. ISBN: 978-0-471-57417-0.
- Tsai, R.E., Seibert, A.F., Eldrige, R.B., Rochelle, G.T., 2011. A dimensionless model for predicting the mass-transfer area of structured packing. AIChE J. 57 (5), 1173–1184. <https://doi.org/10.1002/aic.12345>.
- Westerterp, K.R., van Swaaij, W.P.M., Beenackers, A.A.C.M., 1984. Chemical Reactor Design and Operation. Wiley, New York. ISBN: 0471901830.
- Wu, X., Wang, M., Liao, P., Shen, J., Li, Y., 2020. Solvent-based post-combustion CO₂ capture for power plants: a critical review and perspective on dynamic modelling, system identification, process control and flexible operation. Appl. Energy 257, e113941. <https://doi.org/10.1016/j.apenergy.2019.113941>.
- Ziaii, S., Rochelle, G.T., Edgar, T.F., 2011. Optimum design and control of amine scrubbing in response to electricity and CO₂ prices. Energy Proced. 4, 1683–1690. <https://doi.org/10.1016/j.egypro.2011.02.041>.